CHAPTER 4

COMPARATIVE ENERGETICS ANALYSIS OF CLIMATE MODELS WITH HIGH AND LOW RESOLUTIONS

Hiroshi L. Tanaka and Akira Hasegawa

4.1 Introduction

Global-scale atmospheric motion is excited by solar radiation. The driving force of the radiation has a global scale. Solar energy into the atmospheric system cascades down to smaller scale eddies of high–low pressure systems and, ultimately, to the molecular dissipation processes. Analysis of energy transfer among different scales of motions offers a fundamental understanding of the general circulation of the atmosphere. The operational weather prediction models and the state-of-the-art climate models must be formulated to correctly simulate the energy cascade in the wavenumber spectral domain based on the knowledge of the observational analysis.

The effect of doubled CO_2 and increasing anthropogenic gases will enhance the absorption of solar energy. The anomalous radiative driving force due to the anthropogenic gases would be initiated at the global scale and is expected to cascade down to smaller scale motions, such as high- and low-pressure systems, through the nonlinear wave–wave interactions. The model performance for simulating a new atmospheric equilibrium in response to the anomalous global heating is closely related to the accuracy of energy redistribution over the wide range of the wavenumber spectrum.

Present climate models have relatively coarse horizontal and vertical resolutions due to the inevitable restrictions in computing capability. In the coarse general circulation models, for example R15 (rhomboidally truncated at the total wavenumber 15), the spectral truncation at the medium wavenumber imposes unrealistic restrictions in spectral energy transfer. The nonlinear energy cascade within the model atmosphere must terminate at the imposed truncation wavenumber. In reality, of course, there is no artificial spectral boundary, and the energy input at the large scale is transferred to the dissipation range without interruption. Hence, the examination of the influence of the artificial spectral boundary at the truncation wavenumber upon the climatic equilibrium state is an important research subject in the climate modeling effort. The evaluation of the energy transfer between the large-scale and

63

small-scale motions is the first step in assessing the basic performance of existing climate models.

The diagnosis of spectral energetics has long been performed by a zonal harmonic expansion since the original work by Saltzman (1957, 1970). Kung and Tanaka (1983, 1984) reported the first comprehensive analysis of global energy transformations in the zonal wavenumber domain, using the most extensive worldwide observation of the First GARP (Global Atmospheric Research Program) Global Experiment (FGGE). According to their observational analysis, nonlinear wave–wave interactions of kinetic energy are basically negative for zonal wavenumbers less than 15, indicating that the energy is generated here and transformed from this range to other scales of motions. For wavenumbers larger than 15, the nonlinear wave–wave interactions indicate positive values because the waves receive energy from the large-scale motions. The sum of the nonlinear energy interactions over the entire spectral domain is zero as required from the energy conservation law.

In contrast to the real atmosphere, the nonlinear energy transfer of a coarse resolution climate model is forced to terminate at the truncation wavenumber. Hence, the positive and negative values of the nonlinear energy interactions must be redistributed over the resolvable wavenumbers. This appears to be a serious constraint in the nonlinear energy transfer. The artificial spectral boundary is anticipated to cause a biased response to the doubled CO_2 and anthropogenic activities. Yet, it is not clear how this spectral boundary modifies the spectral energy transfer and how the model's equilibrium is maintained without the accurate energy cascade toward the dissipation range.

The complicated nonlinear wave–wave interactions with subgrid-scale motions have been parameterised by a simple diffusion or a biharmonic diffusion as seen in the NCAR Community Climate Model (CCM). The performance of the diffusion parameterisation has been questioned in its accuracy for the global atmosphere on a rotating spherical earth (e.g. Matsuno 1980). A detailed analysis is necessary to compare the spectral energy transfers in coarse- and fine-resolution models in order to assess the basic performance of the existing climate models.

In order to overcome the limitations of computer memory required for extremely high resolution climate models, an alternative approach has been developed in the field of limited area climate models. For the purpose of conducting regional climate simulations, the methods of nesting a limited area model (LAM) into a large area model (e.g. GCM) have been studied (Giorgi & Mearns 1991; Kida et al. 1991). The nesting procedure can be implemented in a one-way or a two-way interactive mode. In one-way nesting, information from the coarser resolution model is used at the horizontal boundary to drive the higher-resolution regional submodel, but information from the higher-resolution subregion does not feed back into the lower-resolution domain. In two-way nesting, the exchange of information between the lower-resolution and higher-resolution model components occurs interactively and in both directions. The nested LAM-GCM models are mostly based on the one-way nesting procedure. That is, most of nested LAM-GCM models assume that the up-scale signal transfer of the higher-resolution submodel to the lower-resolution domain can be ignored. In the framework of climate prediction for a range of decades of the future,

this assumption of ignoring the two-way signal transfer could be a great danger in achieving a meaningful prediction on small scales. This cannot be justified unless the magnitude of the scale interactions (i.e. wave–wave interactions) is quantified to be small enough. The magnitude of the scale interactions, however, has not been analysed quantitatively with sufficient accuracy in the previous studies. Answering this question may be one of the most urgent requirements in endeavouring to develop a LAM nested in a GCM.

The objective of the present study is to evaluate the basic performance of present climate models with respect to the energy transfer and scale interactions in the wavenumber domain. We have conducted a sequence of diagnostic analyses of climate model simulations with different model resolutions.

First, spectral energy levels of the model atmosphere are compared with observations. The model bias in the energy level will be analysed. Second, the magnitude and direction of the nonlinear wave–wave interactions are computed for model atmospheres with different horizontal resolutions. The nonlinear energy cascade in the high- and low-resolution models are compared with that of the operational analysis with very high resolution models. Third, the variabilities in both the energy level and its interactions are examined for the high wavenumber range near the truncation of the low-resolution model. The characteristics of the variability for high- and low-resolution models are separately analysed. Finally, the effect of the artificial truncation in the wavenumber domain to the energy redistribution of the model atmosphere is discussed. The analyses of energy transfer spectra would provide some useful information to the abovementioned studies of nesting a LAM into a GCM.

4.2 Global gridded data

It is desirable that the models are integrated under the same conditions. The NCAR Community Climate Model version 2 (CCM2) is integrated under the same conditions except for the parameters in the cloud parameterisation under the MECCA project (Hack et al. 1993; Williamson 1993). The CCM2 simulations are appropriate for the main purpose of this study. As the climate models with different horizontal spectral resolutions, the CCM2 are analysed for four types of models using horizontal resolutions of rhomboidal-15 (R15), and triangular–42, –63 and –106 (T42, T63, T106) resolutions, respectively.

Moreover, the same analyses are carried out for the observed atmosphere. As the observed atmosphere, the European Centre for Medium Range Weather Forecasts (ECMWF) analyses data (TOGA Basic level III) for five years during 1986 through to 1990 are used. The discrepancies among the ECMWF, National Meteorological Center (NMC) and Japanese Meteorological Agency (JMA) analyses in the wavenumber domain are reported by Ogasawara (1995) and Tanaka and Kimura (1996), which conclude that the spectral patterns and global energy balances with these operational analyses are sufficiently close to each other.

The present spectral energetics diagnosis requires a complete set of atmospheric state variables of zonal wind speed u (m/s), meridional wind speed v (m/s), vertical p-velocity ω (Pa/s), temperature T (K), geopotential height Z (m), relative humidity RH (%) and surface

pressure p_s (Pa) for instantaneous time intervals (daily values for CCM2). These variables should be given at the longitude–latitude grids over the globe at the vertical pressure levels for the troposphere and stratosphere. The vertical levels prepared by the existing diagnostic code are 1000, 850, 700, 500, 400, 300, 250, 200, 150, 100, 70 and 50 hPa.

The computation of the nonlinear wave–wave interactions requires a considerable amount of CPU time because the nonlinear interactions involve double summations over the whole wavenumbers. Therefore, we analysed for a three-month period in summer and winter of the climate model simulations.

4.3   Description of the spectral energetics

The computational analysis scheme of the standard spectral energetics in the zonal wavenumber domain is based on Saltzman (1957, 1970). Here, the meteorological variables are expanded in zonal harmonics, and the Fourier coefficients are substituted in the governing equations of primitive equations. The primitive equations may be transformed from the space domain to the wavenumber domain expressed by the Fourier expansion coefficients.

Any real, single-valued function $f(\lambda)$, which is piecewise differentiable in the interval $(0, 2\pi)$, may be written in terms of a Fourier representation,

$$f(\lambda, \phi, p, t) = \sum_{n=-\infty}^{\infty} F(n, \phi, p, t)e^{in\lambda} \tag{1}$$

where the complex coefficients, $F(n)$, are given by

$$F(n, \phi, p, t) = \frac{1}{2\pi} \int_0^{2\pi} f(\lambda, \phi, p, t)e^{-in\lambda}d\lambda \tag{2}$$

We consider the Fourier representation of meteorological variables specified along a given latitudinal circle. Thus, λ is taken as longitude, n is the wavenumber around the latitude circle. The functions $f(\lambda)$ and $F(n)$ to be considered here are listed as follows:

$$f(\lambda) \quad u \ v \ \omega \ Z \ T \ h \ x \ y \quad : \quad \text{space domain}$$

$$F(n) \quad U \ V \ \Omega \ A \ B \ H \ X \ Y \quad : \quad \text{wavenumber domain}$$

Here, h, x, y designate diabatic heating rate, external mechanical force with respect to the east–west direction, and that of the north–south direction, respectively. Since atmospheric kinetic energy and available potential energy are proportional to the wind and temperature variances, the zonal mean energy can be decomposed in contributions from every zonal wavenumber by means of the Parseval's theorem.

$$\frac{1}{2\pi} \int_0^{2\pi} \frac{1}{2}(u^2 + v^2)d\lambda = \sum_{n=-\infty}^{\infty} (|U(n)|^2 + |V(n)|^2) \tag{3}$$

$$\frac{1}{2\pi} \int_0^{2\pi} \frac{1}{2}C_p\gamma T''^2 d\lambda = \sum_{n=-\infty}^{\infty} C_p\gamma |B(n)|^2 \tag{4}$$

Energy equations are then constructed for every zonal wavenumber by differentiating (3) and (4) with respect to time (t), which describes how the temporal variation of wave energy occurs.

We can form a set of equations for the rates of change of the globally integrated kinetic energy and available potential energy in the zonally averaged component (wavenumber zero) and in each of the eddy components corresponding to nonzero wavenumbers. These equations can be written as follows:

$$\frac{dK(0)}{dt} = \sum_{n=1}^{\infty} M(n) + C(0) - D(0)$$

$$\frac{dK(n)}{dt} = -M(n) + L(n) + C(n) - D(n) \quad (n = 1, 2, 3, \dots)$$

$$\frac{dP(0)}{dt} = \sum_{n=1}^{\infty} R(n) - C(0) + G(0)$$

$$\frac{dP(n)}{dt} = -R(n) + S(n) - C(n) + G(n) \quad (n = 1, 2, 3, \dots) \tag{5}$$

Definitions of integrals appearing in (5) are written as follows, where all quantities are measured per unit mass:

total kinetic energy in eddies of wavenumber n,

$$K(n) = \langle(|U(n)|^2 + |V(n)|^2)\rangle$$

total kinetic energy in zonally averaged motions,

$$K(0) = \frac{1}{2}\langle[u]^2 + [v]^2\rangle,$$

total available potential energy in eddies of wavenumber n,

$$P(n) = \langle C_p\gamma |B(n)|^2\rangle,$$

where

$$\gamma = \left(\tilde{T} - \frac{c_p p}{R}\frac{d\tilde{T}}{dp}\right)^{-1},$$

total available potential energy in zonally averaged temperature distribution,

$$P(0) = \frac{1}{2}\langle C_p \gamma \{[T]''^2\}\rangle,$$

where the symbol $\langle\rangle$ designates a mass integral over the entire mass of the atmosphere.

This kinetic energy equation represents that the energy variation is caused by its zonal-wave interactions $M_{(n)}$, wave–wave interactions $L_{(n)}$, baroclinic conversion $C_{(n)}$, and energy dissipation $D_{(n)}$. Available potential energy equation is also represented by its zonal-wave interactions $R_{(n)}$, wave–wave interactions $S_{(n)}$, baroclinic conversion $C_{(n)}$, and diabatic heat sources and sinks $G_{(n)}$. Evaluating those energetic terms from the gridded data, the energy spectra and energy transformations can be examined over the wavenumber domain.

The energy transformations are defined as follows:

baroclinic conversion from available potential energy of wavenumber n to kinetic energy of wavenumber n,

$$C(n) = -\left\langle\frac{R}{p}[B(n)\Omega(-n) + B(-n)\Omega(n)]\right\rangle,$$

baroclinic conversion from zonal available potential energy to zonal kinetic energy,

$$C(0) = -\left\langle\frac{R}{p}\{[T]''[\omega]''\}\right\rangle,$$

zonal-wave interaction of kinetic energy from eddies of wavenumber n to the zonally averaged flow,

$$M(n) = M_1(n) + M_2(n) + M_3(n),$$

where

$$M_1(n) = \left\langle[U(n)V(-n) + U(-n)V(n)]\frac{\cos\phi}{a}\frac{d}{d\phi}\left(\frac{[u]}{\cos\phi}\right)\right\rangle$$

$$M_2(n) = \left\langle[U(n)\Omega(-n) + U(-n)\Omega(n)]\frac{d[u]}{dp}\right\rangle$$

$$M_3(n) = \left\langle 2[V(n)V(-n)]\frac{\partial[v]}{a\partial\phi} + [V(n)\Omega(-n) + V(-n)\Omega(n)]\frac{d[v]}{dp}\right.$$

$$\left. -2[U(n)U(-n)][v]\frac{\tan\phi}{a}\right\rangle,$$

zonal-wave interaction of available potential energy from eddies of wavenumber n to the zonally averaged field,

$$R(n) = R_1(n) + R_2(n),$$

where

$$R_1(n) = \left\langle C_p \gamma [B(-n)V(n) + B(n)V(-n)] \frac{\partial [T]}{a \partial \phi} \right\rangle,$$

$$R_2(n) = \left\langle C_p \gamma \left(\frac{p}{p_s}\right)^k \left\{ [B(-n)\Omega(n) + B(n)\Omega(-n)]'' \frac{d[O]''}{dp} \right\} \right\rangle,$$

wave–wave interactions of kinetic energy for wavenumber n from eddies of all wavenumbers,

$$L(n) = L_1(n) + L_2(n), \quad \left(\sum_{n=1}^{\infty} L(n) = 0 \right),$$

where

$$L_1(n) = -\left\langle \sum_{\substack{m=-\infty \\ \neq 0}}^{\infty} \frac{in}{a \cos \phi} (U(m)[U(-n)U(n-m) - U(n)U(-n-m)] \right.$$

$$+ V(m)[V(-n)U(n-m) - V(n)U(-n-m)])$$

$$+ \frac{1}{a \cos \phi} \left(U(-n) \frac{d}{d\phi} [U(m)V(n-m) \cos \phi] \right.$$

$$+ U(n) \frac{d}{d\phi} [U(m)V(-n-m) \cos \phi]$$

$$+ V(-n) \frac{d}{d\phi} [V(m)V(n-m) \cos \phi] + V(n) \frac{d}{d\phi} [V(m)V(-n-m) \cos \phi] \right)$$

$$- \frac{\tan \phi}{a} (V(m)[U(-n)U(n-m) + U(n)U(-n-m)] - U(m)[V(-n)U(n-m)$$

$$+ V(n)U(-n-m)]) \rangle,$$

$$L_2(n) = -\left\langle \sum_{\substack{m=-\infty \\ \neq 0}}^{\infty} \left(U(-n) \frac{d}{dp} [U(m)\Omega(n-m)] + U(n) \frac{d}{dp} [U(m)\Omega(-n-m)] \right. \right.$$

$$+ V(-n) \frac{d}{dp} [V(m)\Omega(n-m)] + V(n) \frac{d}{dp} [V(m)\Omega(-n-m)] \right) \rangle,$$

wave–wave interactions of available potential energy for wavenumber n from eddies of all wavenumbers,

$$S(n) = S_1(n) + S_2(n), \quad \left(\sum_{n=1}^{\infty} S(n) = 0 \right),$$

where

$$S_1(n) = \left\langle C_p \gamma \sum_{\substack{m=-\infty \\ \neq 0}}^{\infty} \left(\frac{in}{a \cos \phi} B(m)[B(-n)U(n-m) - B(n)U(-n-m)] \right. \right.$$

$$\left. \left. + \frac{B(m)}{a} \left[V(n-m) \frac{d}{d\phi} B(-n) + V(-n-m) \frac{d}{d\phi} B(n) \right] \right) \right\rangle,$$

$$S_2(n) = -\left\langle C_p \gamma \sum_{\substack{m=-\infty \\ \neq 0}}^{\infty} \left(B(m) \left[\Omega(n-m) \left(\frac{dB(-n)}{dp} - \frac{RB(-n)}{c_p p} \right) \right. \right. \right.$$

$$\left. + \Omega(-n-m) \left(\frac{dB(n)}{dp} + \frac{RB(n)}{c_p p} \right) \right]$$

$$\left. \left. - \frac{d}{dp} (B(m)[B(-n)\Omega(n-m) + B(n)\Omega(-n-m)]) \right) \right\rangle,$$

rate of viscous dissipation of the kinetic energy for wavenumber n,

$$D(n) = -\langle [U(n)X(-n) + U(-n)X(n)] + [V(n)Y(-n) + V(-n)Y(n)] \rangle,$$

rate of viscous dissipation of the zonal kinetic energy,

$$D(0) = -\langle ([u][x] + [v][y]) \rangle,$$

rate of generation of available potential energy of wavenumber n due to diabatic heating,

$$G(n) = \langle \gamma[B(n)H(-n) + B(-n)H(n)] \rangle,$$

rate of generation of zonal available potential energy due to zonally averaged heating,

$$G(0) = \langle \gamma \{ [T]''[h]'' \} \rangle.$$

By evaluating these energetics terms, Saltzman showed, first, that the atmospheric kinetic energy is generated at the synoptic scale of zonal wavenumbers 6–10 by the synoptic disturbances and that the energy is transferred to both planetary waves and short waves. The energy transfer toward the short wavelengths corresponds to the downscale energy cascade to the dissipation range, whereas the transfer toward the large-scale (up-scale cascade) feeds

the energy of the planetary waves and zonal jet stream in the atmosphere. If we sum the equations over all wavenumbers, excluding wavenumber zero, noting that $\sum_{n=1}^{\infty} L(n) = 0$; $\sum_{n=1}^{\infty} S(n) = 0$, we obtain a set of equations similar to that derived by Lorenz (1955) and reviewed by Oort (1964) under the name of 'space domain equations'.

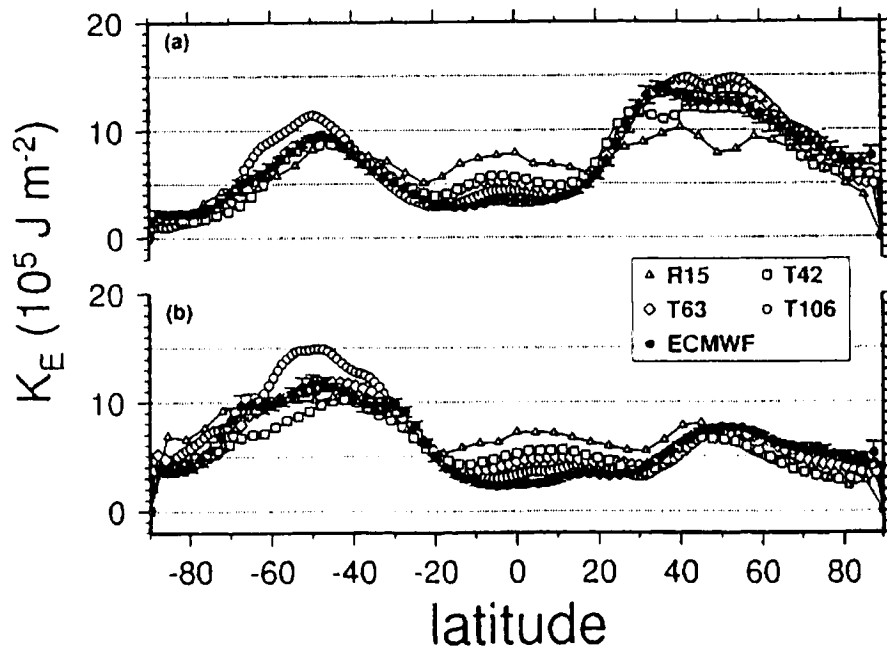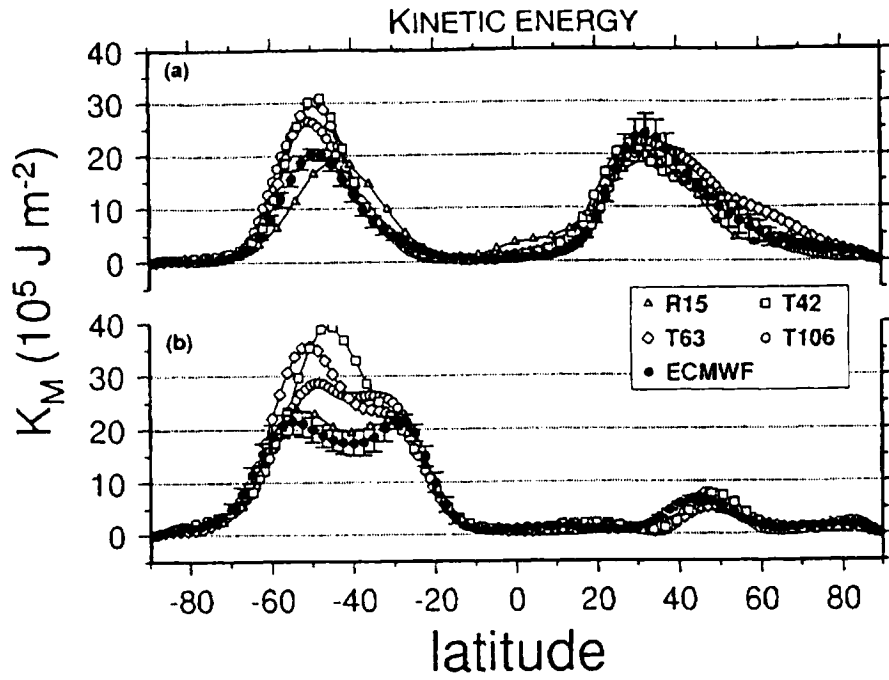## 4.4   Meridional distribution of kinetic energy

Comprehensive description of the spectral energetics analysis of this study is summarised in Hasegawa (1995). Some selected results of the analysis, especially for kinetic energy balance, are documented in the following figures.

Figure 4.1 illustrates the meridional distributions of zonal and eddy kinetic energy for the CCM2 and ECMWF datasets during (a) northern winter and (b) summer. Local discrepancies in K_M, i.e. $\bar{u}$ fields, between the ECMWF analysis and CCM2 simulations are evident. Zonal kinetic energy K_M in the CCM2 is significantly overestimated in the SH middle latitudes. In other words, the jet is too strong in the model. The discrepancies of K_M are much more significant in the winter SH than in the summer SH. The black dot denotes an observed mean level by the ECMWF analysis, and the standard deviation for the five-year analysis period is marked by a deviation bar around the black dot. In the winter SH, the CCM2 simulations, except for T42, represent two-maxima of K_M in the middle latitudes (Figure 4.1 (b)). These features of the simulated atmosphere are related to the double-jet structure produced by the subtropical jet and polar frontal jet. The double-jet structure is completely missing in T42. In the SH middle latitude, zonal-wave interactions of K in the CCM2 is stronger than in the observations, that is, the CCM2 transfers much momentum from eddies to the zonal mean field and intensifies the westerly wind. The minimum value of M in the SH middle latitudes is not well simulated in the CCM2-T42.

The eddy kinetic energy K_E simulated with the CCM2 is larger than that in the ECMWF analysis in the tropics. This bias results from both large M and C_E in simulations near the equator. The CCM2 circulation, moreover, transfers a large amount of kinetic energy from zonal mean into eddies ($K_M \rightarrow K_E$) in the winter hemisphere at low latitudes.

4.5   Vertical distribution of kinetic energy

Figure 4.2 illustrates the vertical distributions of zonal and eddy kinetic energy for the CCM2 and ECMWF datasets during (a) northern winter and (b) summer. The vertical structures of K_M indicate interesting difference in the stratosphere between northern winter (DJF) and summer (JJA). For DJF the mean level of the tropopause is seen at about 200 hPa level, and the energy level decreases in the stratosphere. For JJA, in contrast, the energy level is approximately constant in the stratosphere. The difference seems to come from the different intensity of the polar night jet and the polar frontal jet. The polar night jet in the middle atmosphere extends downward and is connected with a clear polar frontal jet in the winter SH. Although the same polar night jet exists in the winter NH, it does not extend to low levels and the polar frontal jet is not detected in the winter NH in the mean.

Figure 4.1 Meridional distribution of zonal kinetic energy K_M and eddy kinetic energy K_E for CCM2 and ECMWF datasets during (a) northern winter and (b) summer.

Figure 4.2 Vertical distribution of zonal kinetic energy K_M and eddy kinetic energy K_E for CCM2 and ECMWF datasets during (a) northern winter and (b) summer.

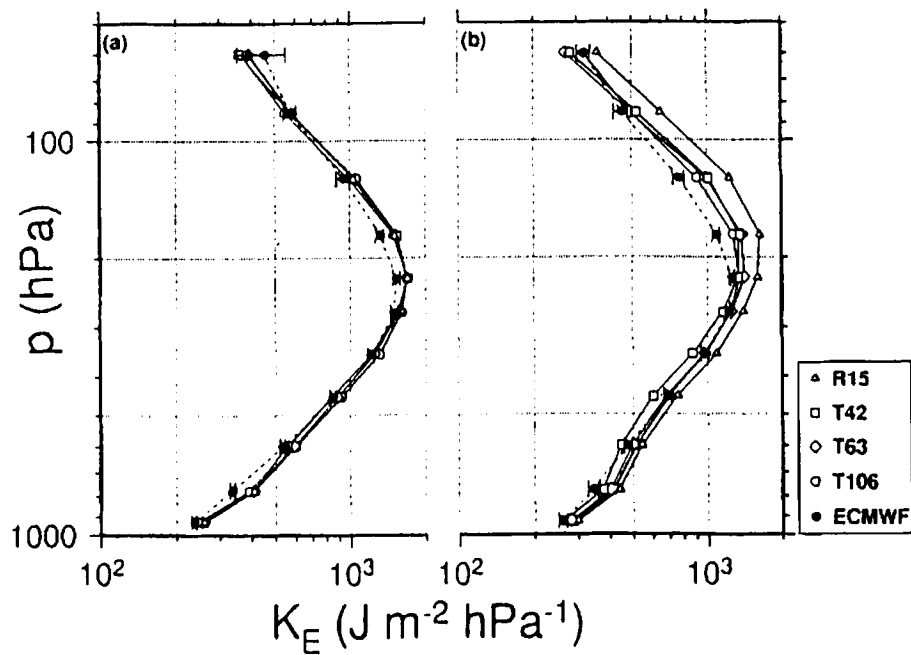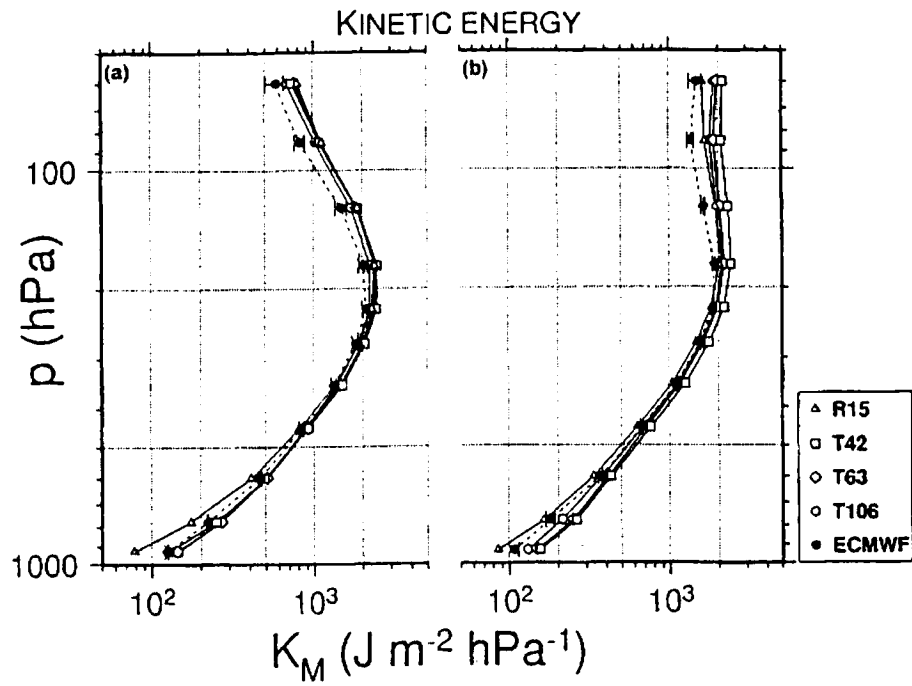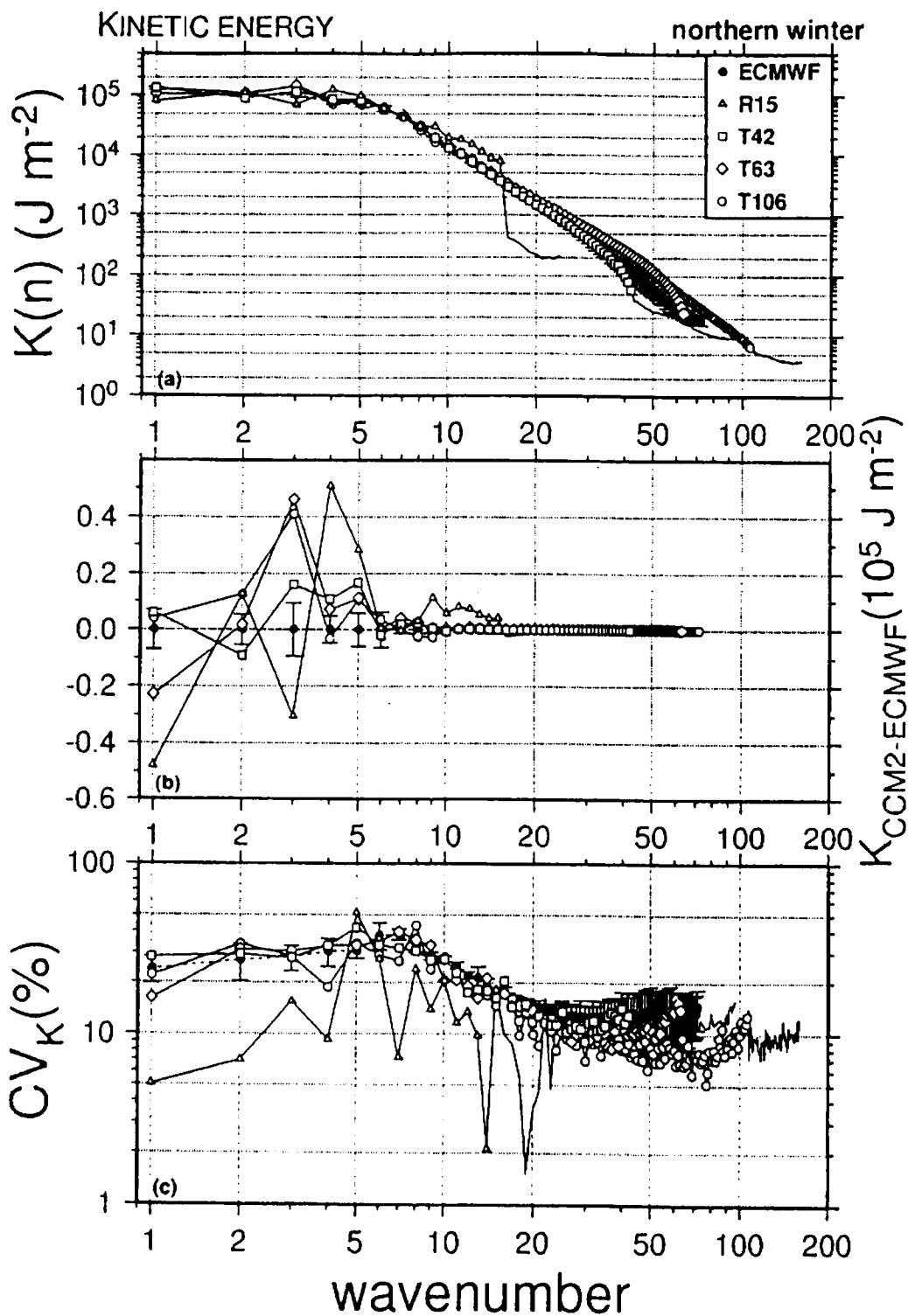**Figure 4.3** Spectral distribution of kinetic energy K_n for CCM2 and ECMWF datasets during northern winter and summer; (a) spectral distribution, (b) deviation from ECMWF analysis, (c) coefficient of variation.
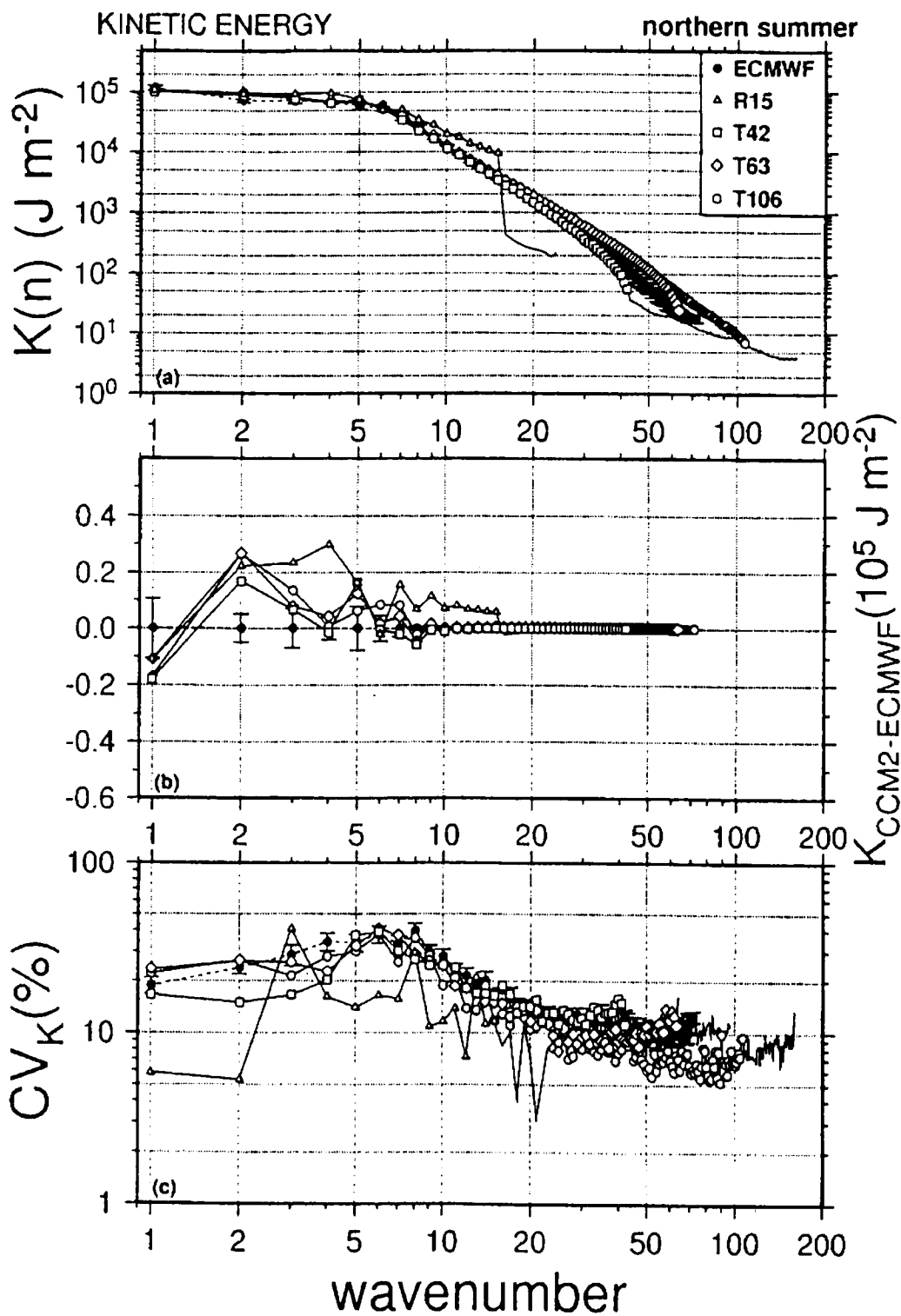
Figure 4.3 *(continued)*

Minor discrepancies are seen in the stratosphere in K_M fields between the ECMWF analysis and CCM2 simulations. The jet is generally stronger in CCM2 above the tropopause. In the troposphere, the agreement between the model and observations is rather good.

The vertical profile of K_E indicates a peak at about 250 hPa level. The peak coincides approximately with the tropopause level. The contrast between DJF and JJA is slight, showing an insignificant seasonality. The CCM2 simulations show almost a perfect fit for the northern winter, but the difference is large for the northern summer. The CCM2, especially R15, indicates excessive eddies above the tropopause level.

4.6   Spectral distribution of kinetic energy

Spectral distributions of kinetic energy K_n for the northern winter and summer are presented for CCM2 simulations and the ECMWF analysis in Figure 4.3. The upper panel of the figure illustrates the energy spectrum. The black dots are for ECMWF analysis while white symbols are for CCM2 simulations. The symbols are plotted up to the model's truncation wavenumber. No symbols are plotted beyond that wavenumber although the analysis wavenumber extends a little more depending on the gridded size of the globally interpolated data. The energy level drops by more than an order of magnitude for R15 at the zonal wavenumber 15, as is expected. The spectral slope is flat for wavenumbers 1 to about 5 and it becomes red beyond the wavenumber 5, showing a -3 power law of the 2–D or geostrophic turbulence. The CCM2 spectrum coincides with that of ECMWF except for R15 which indicates higher biases in the energy level near the truncation wavenumber.

The difference between the CCM2 simulations and ECMWF observations are plotted in the middle panel of the figure with a linear scale on the ordinate. The standard deviation bars are marked for the black symbols of ECMWF. Since the standard deviations evaluated from the time series are only about 0.1 (10^5 Jm^{-2}), almost all CCM2 simulations lie outside the standard deviation bars. Namely, the differences in the energy levels between the models and observations are significant for all simulations.

The lower panel of the figure illustrates a spectrum of the coefficient of variation, defined as the standard deviation in the time series divided by its time average. The largest value of the coefficient of variation is about 40% at the synoptic scale. The values are reduced to about 30% for the planetary waves and to 10% for short waves. It is interesting to note that the time variation for R15 is reduced consistently for almost all waves. This may be a good example to remember that the characteristics in time variation could be biased from reality for a highly truncated model, even though the climatology can be tuned at the right order.

The comparison of the results for the northern winter and summer shows that the spectral characteristics are similar to each other. The results for R15 are clearly biased from the observations. The discrepancies tend to diminish as the resolution increases.

4.7   Spectral distribution of energy transformations

Figure 4.4 illustrates the spectral distribution of baroclinic conversion $C_{(n)}$ for CCM2 and ECMWF datasets during the northern winter and summer. The baroclinic conversion
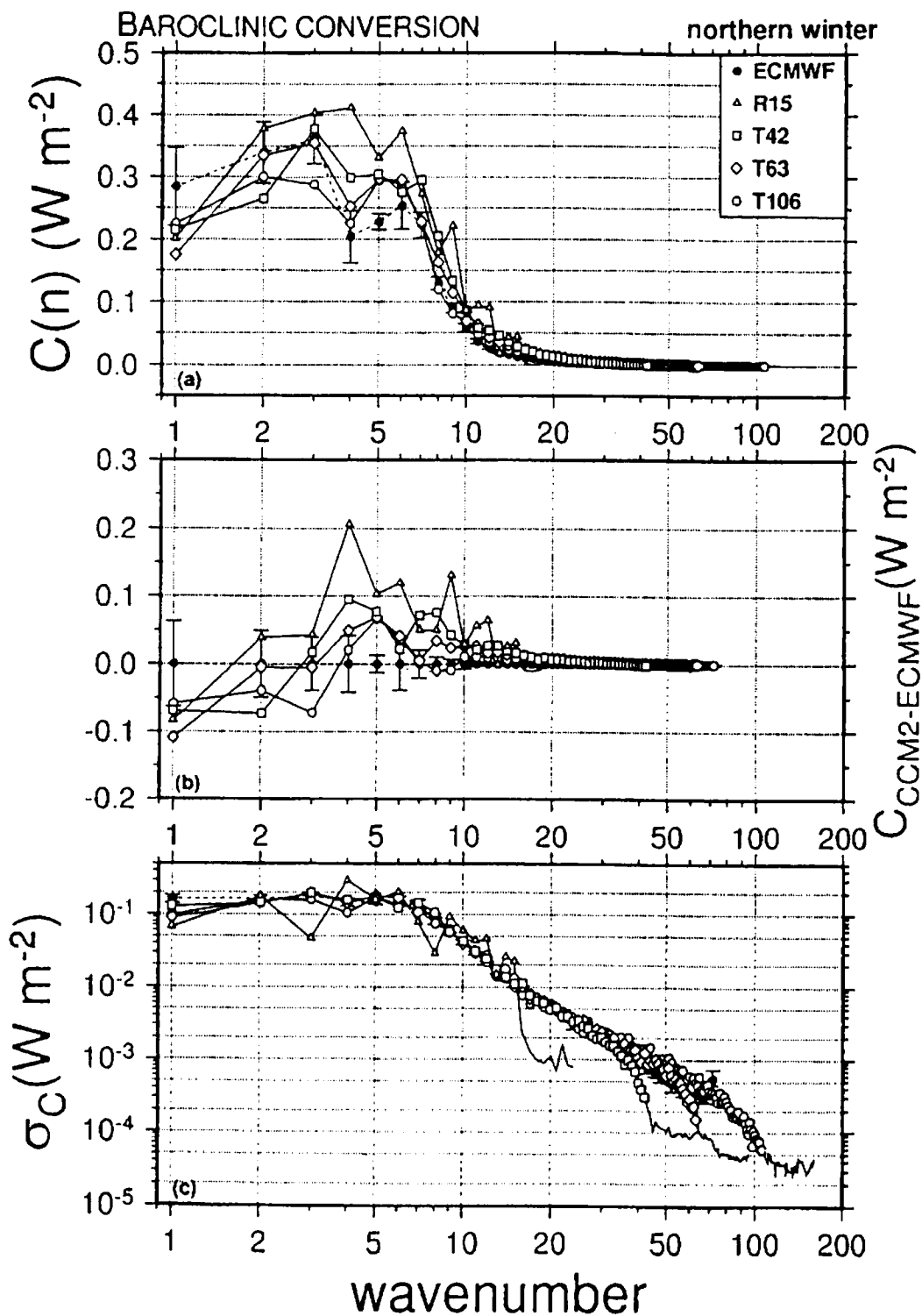
Figure 4.4 Spectral distribution of baroclinic conversion C_n for CCM2 and ECMWF datasets during northern winter and summer; (a) spectral distribution, (b) deviation from ECMWF analysis, (c) standard deviation of the time variation.
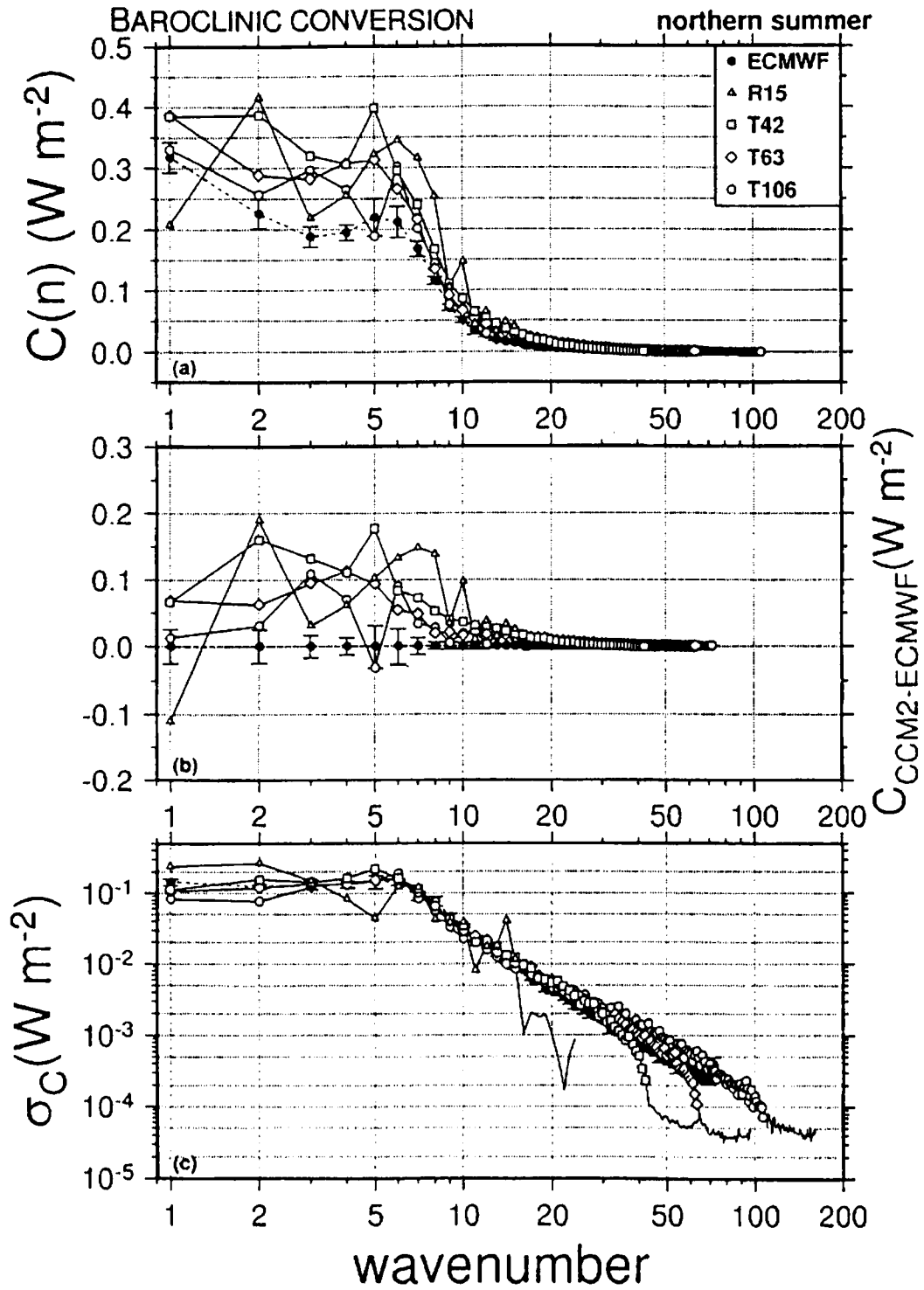
Figure 4.4 *(continued)*

from $P_{(n)}$ to $K_{(n)}$ is large at planetary waves and another peak is seen in the synoptic waves. According to the middle panel of the figure, this term is overestimated by CCM2 for almost all waves except for wavenumber 1 in the northern winter. The lower panel shows the spectrum of the standard deviation in the time series. It is noteworthy that the standard deviation is flat at the wavenumbers 1 to 6 and it decreases at the short wavelengths, showing a red spectrum with a slope of –3. The spectral characteristics observed in this energy transformation is quite similar to those in the energy spectrum itself in Figure 4.3.
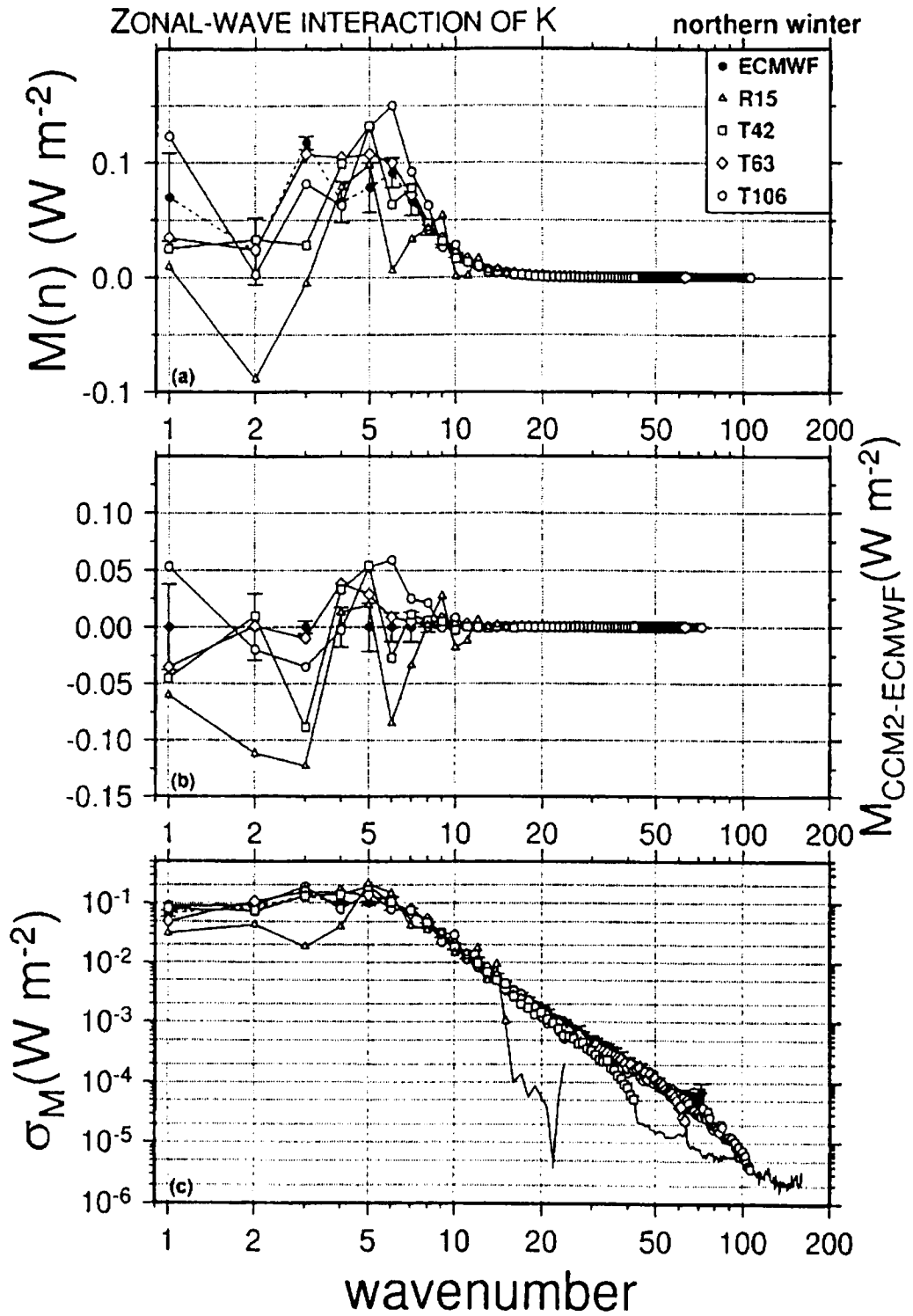
Figure 4.5 illustrates the spectral distribution of zonal-wave interactions $M_{(n)}$ for CCM2 and ECMWF datasets during the northern winter and summer. The zonal-wave interactions are large for synoptic waves, which accelerate zonal motions. The model biases are greater than the standard deviation bars of ECMWF. As illustrated in Figure 4.4, the standard deviation of the time variation indicates a red spectrum beyond the synoptic wavenumbers.

Figure 4.6 illustrates the spectral distribution of wave–wave interactions $L(n)$ for CCM2 and ECMWF datasets during the northern winter and summer. This term is important for assessment of the magnitude of the scale interactions between the large and small. The term is negative at synoptic wavelengths, indicating an energy supply at this scale through baroclinic conversion. The values are positive both for planetary waves and short waves, showing that the energy is transferred from the source range to both planetary waves and short waves. There is an exception in which the value is negative at the wavenumber 2 of the northern winter. There is another type of energy source at the wavenumber 2 in the northern winter, which may be a topographic excitation of wavenumber 2.

The result of differences between CCM2 and ECMWF in the middle panel shows that the bias in R15 is unacceptable. In theory, the wave–wave interactions must be zero when summed over all the waves from one to infinity. The observed wave–wave interactions indicate negative values for synoptic waves up to the wavenumber of about 15. These negative values are compensated partly by the small positive values at large wavenumbers. This process is referred to as downscale energy transfer from synoptic waves to short waves. However, when the wavenumber is truncated at 15 in the model atmosphere as in R15, the important downscale energy cascade is forbidden. This is a strong restriction and a distortion from the reality. As a result, the wave–wave interactions for R15 indicate negative values up to wavenumber 10 and they are compensated by the unrealistic positive values at wavenumbers 10–15. The energy redistribution is evidently distorted by the artificial spectral boundary at R15.

The distortion in the wave–wave interactions become even clearer when the interaction terms are integrated with respect to the wavenumbers. The integral function is regarded as an energy flux in the wavenumber domain. Since the summation of the interactions for all waves becomes zero as required from the energy conservation law, the energy flux will converge to zero as the wavenumber approaches infinity. This physical constraint is attained at the finite wavenumbers when a model atmosphere is truncated at a finite wavenumber. For example, the energy flux must converge to zero at wavenumber 15 for the case of R15.

Figure 4.7 illustrates the energy flux over the wavenumber domain evaluated for CCM2 and ECMWF datasets during the northern winter and summer. The results for ECMWF

Figure 4.5 Spectral distribution of zonal-wave interaction of kinetic energy M_n for CCM2 and ECMWF datasets during northern winter and summer; (a) spectral distribution, (b) deviation from ECMWF analysis, (c) standard deviation of the time variation.

Figure 4.5 *(Continued)*

Figure 4.6 Spectral distribution of wave–wave interaction of kinetic energy L_n for CCM2 and ECMWF datasets during northern winter and summer; (a) spectral distribution, (b) deviation from ECMWF analysis, (c) standard deviation of the time variation.
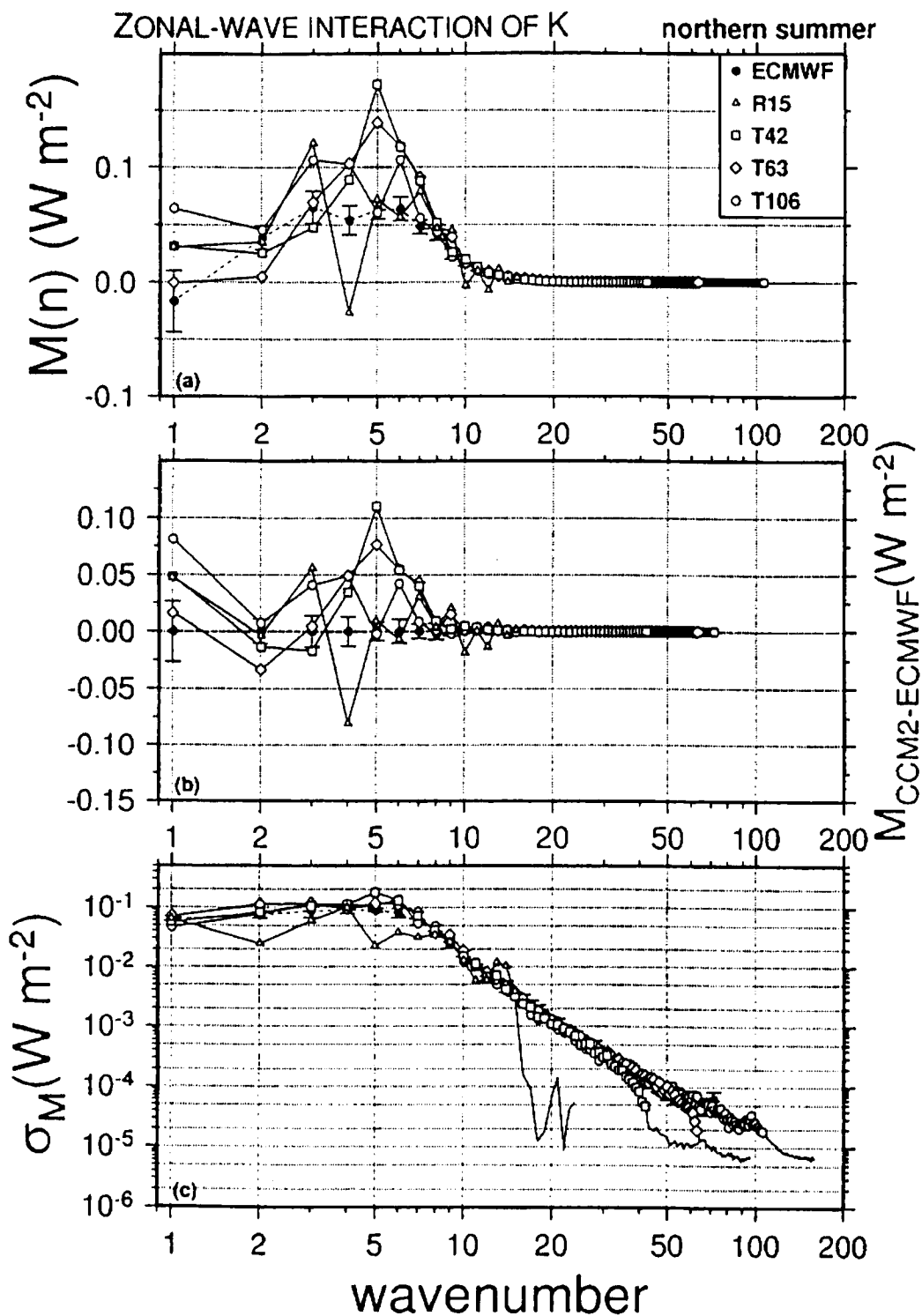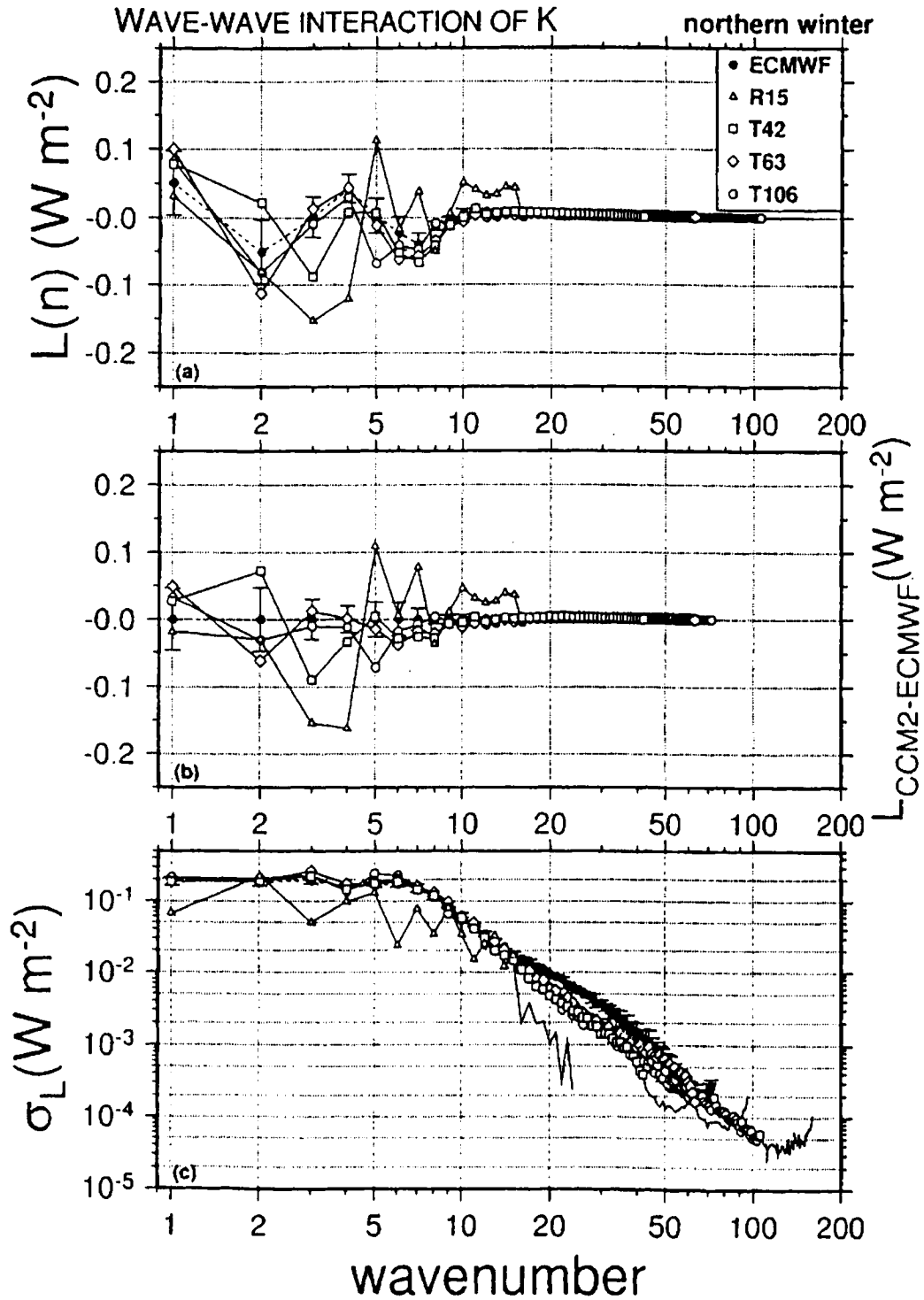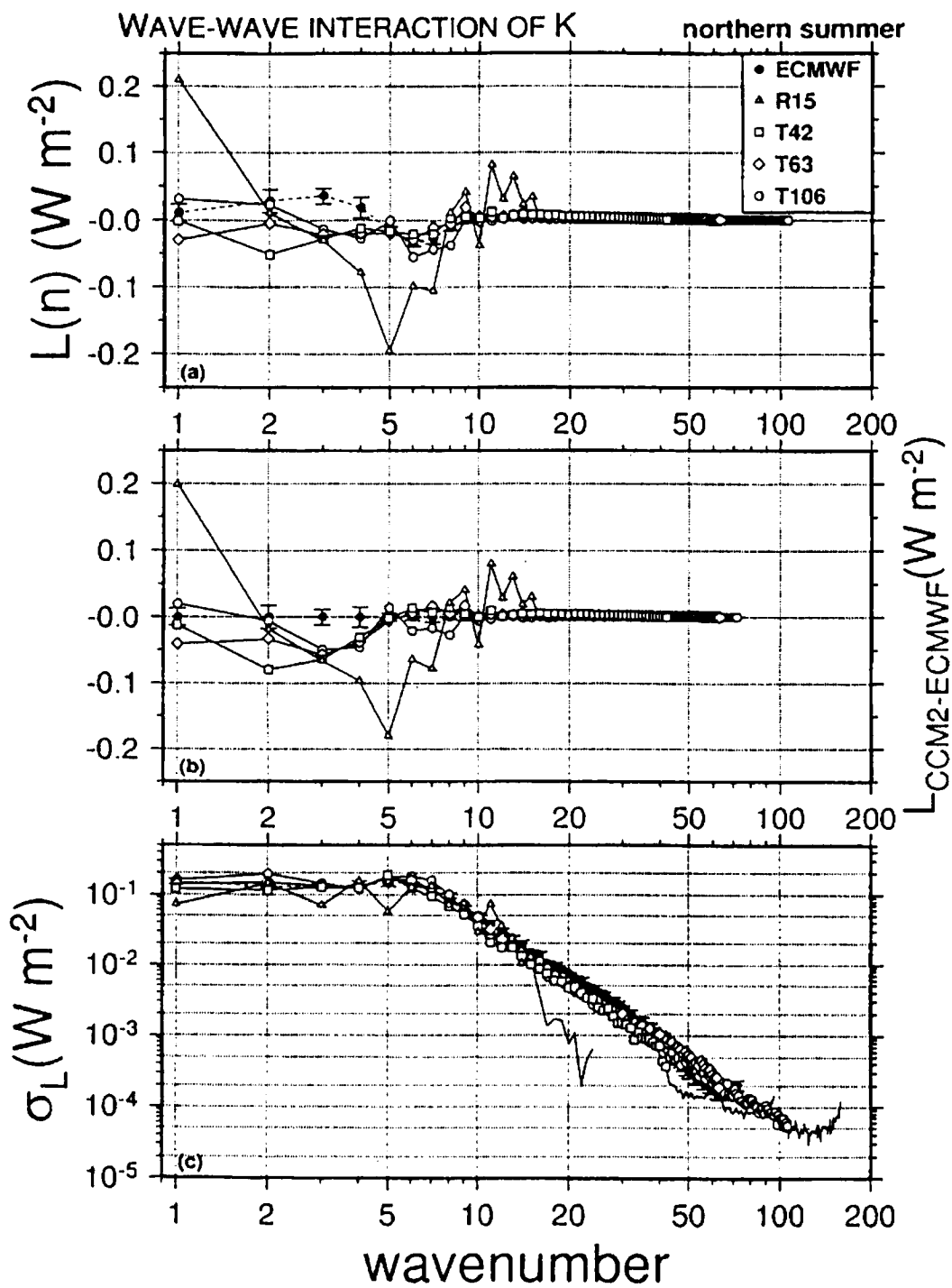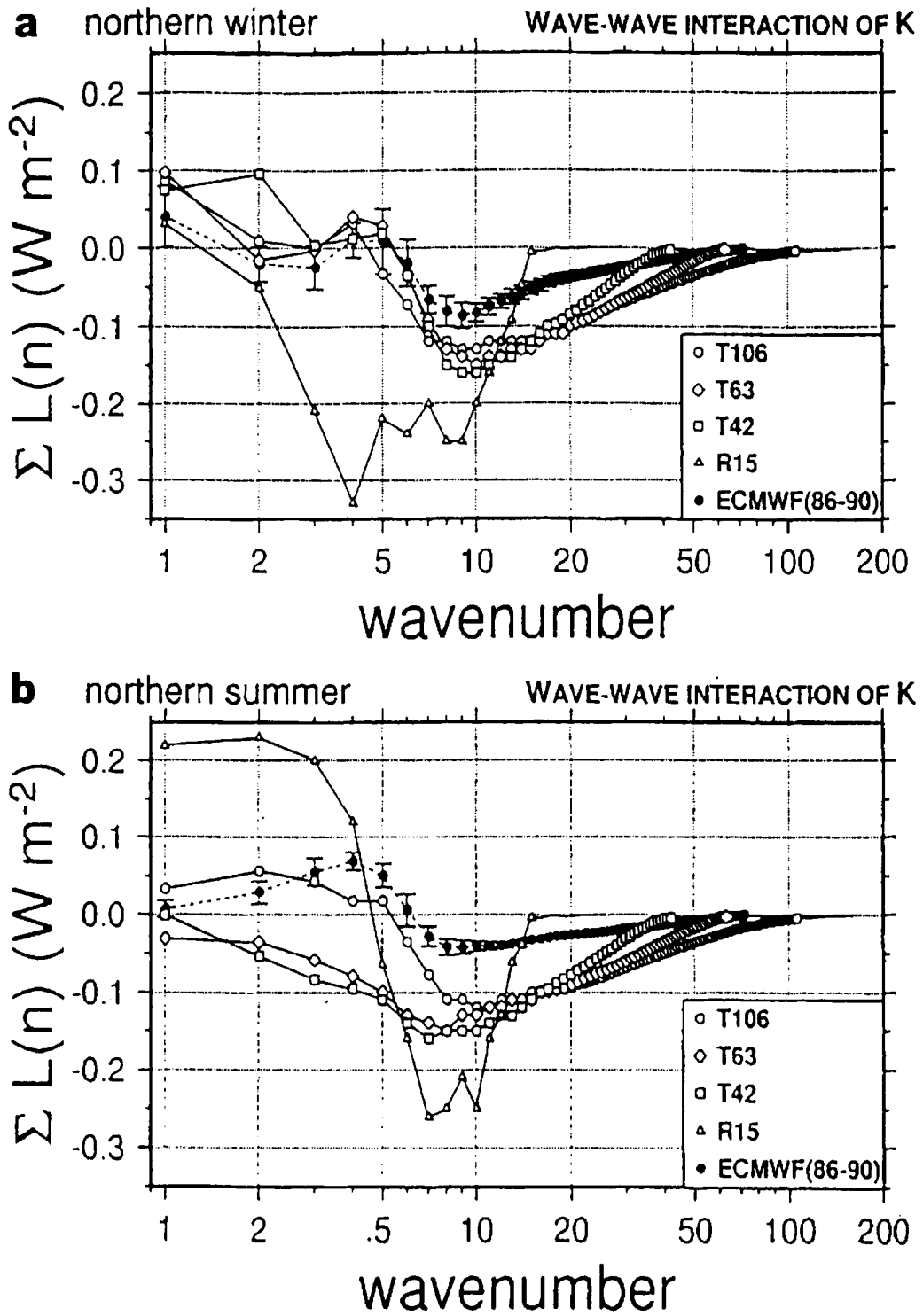
Figure 4.6 *(Continued)*

Figure 4.7 Spectral distribution of kinetic energy flux in the wavenumber domain $\sum L_n$ for CCM2 and ECMWF datasets during (a) northern winter and (b) summer.

indicate a zero crossing at the wavenumber 6 and negative values for larger wavenumbers. This implies that the energy is transferred toward larger wavenumbers (smaller scale motions). This is the flux associated with the downscale energy cascade, and the energy is transferred to smaller scale motions. When a large vortex breaks down to a number of smaller vortex and the smaller vortex breaks down to a further smaller vortex, the energy cascades down to smaller scale motions. The largest flux is seen at wavenumber 10, and the magnitude is about 0.1 W m^{-2} for the northern winter result. In the planetary waves, the values are, in general, positive as typically seen in the northern summer. In this case the energy flux directs towards the small wavenumbers (larger scale motions). This is the flux associated with the upscale energy cascade, and the energy is transferred to larger scale motions. The flux divergence represents an energy source, whereas the flux convergence represents an energy sink. Evidently, there is a large source at the synoptic scale near the zero crossing of the line where the flux strongly diverges.

Now, the results for CCM2 qualitatively indicate similar distributions of the flux as ECMWF, but the magnitudes are twice as larger for T42, T63 and T106. The result for T106 converges to zero at wavenumber 106. Similarly, the results for T63, T42 and R15 converges to zero at wavenumbers 63, 42 and 15. The energy redistribution must occur within these spectral ranges. The distortion in R15 is terrible. At the wavenumber 15 the other resolution models indicate a downscale energy flux of about 0.1 W m^{-2}. However, this flux is forced to zero in R15. The upscale energy cascade observed for the northern summer is missing in T42 and T63. Only T106 reproduces the upscale energy cascade.

4.8 Energy flow diagram

The result of the spectral energetics is summarised in the form of Saltzman's box diagram (refer to Kung 1988). Here, the kinetic energy $K_{(n)}$ and available potential energy $P_{(n)}$ are listed in the energy boxes and the energy transformations of $R_{(n)}$, $S_{(n)}$, $C_{(n)}$, $L_{(n)}$, and $M_{(n)}$ are indicated by arrows. The energy generation $G_{(n)}$ and dissipation $D_{(n)}$ are evaluated as the residual balances of the energy equations. Figure 4.8 is for the result of T106 of CCM2 during the northern winter and summer. For convenience and for simplicity, the energy boxes are combined for wavenumbers 1–3, 4–7, 8–15, 16–42, 43–63, 64–72, 73–106 and 107–160. If we sum all waves for 1–160, the resulting 4 energy box diagram is reduced to a Lorenz energy box diagram (see Lorenz 1955).

The main entrance of the atmospheric energy into the Saltzman's box diagram is at the differential heating $G_{(o)}$, where the warmer tropics are heated and the colder polar regions are cooled. Zonal available potential energy $P_{(o)}$ is excited by the differential heating with increased meridional temperature gradients. The increased meridional temperature gradients will induce baroclinic instability where warm air rises and is transported to high latitudes and cold air sinks and is transported to lower latitudes. This process is indicated by the zonal-wave interactions $R_{(n)}$ and the baroclinic conversion $C_{(n)}$. With the typical energy flow of the baroclinic instability, $K_{(n)}$ is excited mostly at the synoptic scale.

a   **CCM2-T106**   **northern winter**

2.10E+00   -2.18E-02   7.77E-01

2.12E+00   5.28E+06   8.35E+05   7.98E-01

n= 0   n= 0

G(n)   R(n)   P(n)   S(n)   C(n)   L(n)   K(n)   M(n)   D(n)

7.88E-01   8.13E-01   2.08E-01

1.03E-01   4.47E+05   -7.83E-02   -8.20E-03   3.86E+05   5.97E-01

n= 1- 3   n= 1- 3

1.07E+00   1.04E+00   4.35E-01

4.04E-02   1.59E+05   -7.21E-02   -1.27E-01   2.56E+05   4.74E-01

n= 4- 7   n= 4- 7

2.35E-01   4.30E-01   1.52E-01

1.01E-01   4.78E+04   9.35E-02   -1.30E-04   8.70E+04   2.78E-01

n= 8- 15   n= 8- 15

2.66E-02   1.88E-01   8.46E-03

9.47E-02   1.98E+04   6.69E-02   6.55E-02   2.35E+04   2.45E-01

n= 16- 42   n= 16- 42

3.77E-03   3.30E-02   -3.16E-03

1.64E-02   3.40E+03   1.29E-02   2.32E-02   2.02E+03   5.94E-02

n= 43- 63   n= 43- 63

7.32E-04   8.15E-03   -5.32E-04

2.73E-03   8.42E+02   4.69E-03   6.35E-03   3.24E+02   1.50E-02

n= 64- 72   n= 64- 72

1.70E-03   1.51E-02   -7.49E-04

1.96E-03   2.02E+03   1.14E-02   1.10E-02   4.95E+02   2.68E-02

n= 73-106   n= 73-106

1.59E-03   7.08E-03   -2.37E-04

7.76E-03   1.96E+03   -2.27E-03   3.62E-03   2.35E+02   1.09E-02
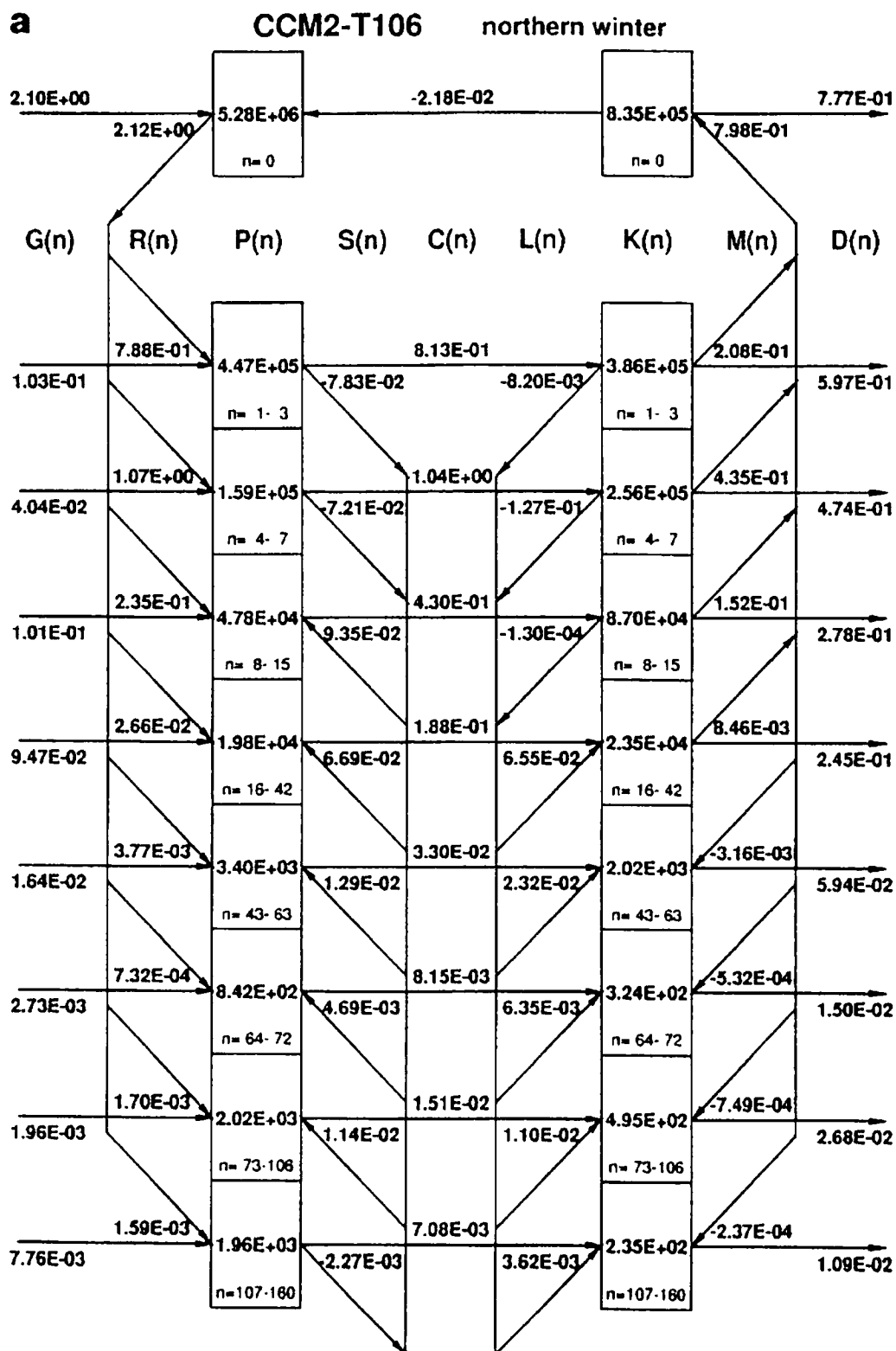
n=107-160   n=107-160

Figure 4.8 Energy flow diagram in the wavenumber domain for the CCM2-T106 simulation during (a) northern winter and (b) northern summer.

b   **CCM2-T106**   **northern summer**

1.75E+00

4.71E+06   -3.78E-02   7.78E+05   6.17E-01

1.79E+00   n= 0   6.55E-01

n= 0

G(n)   R(n)   P(n)   S(n)   C(n)   L(n)   K(n)   M(n)   D(n)

5.67E-01   3.58E+05   8.85E-01   2.87E+05   2.17E-01

3.70E-01   5.18E-02   3.96E-02   7.08E-01

n= 1- 3   n= 1- 3

9.83E-01   1.35E+05   9.57E-01   2.38E+05   3.26E-01

4.43E-02   7.08E-02   -1.28E-01   5.03E-01

n= 4- 7   n= 4- 7

2.04E-01   4.63E+04   4.68E-01   8.40E+04   1.15E-01

1.42E-01   1.22E-01   -2.88E-02   3.24E-01

n= 8- 15   n= 8- 15

2.61E-02   2.10E+04   2.39E-01   2.43E+04   3.52E-03

1.22E-01   9.06E-02   5.43E-02   2.90E-01

n= 16- 42   n= 16- 42

1.81E-03   3.81E+03   4.14E-02   2.05E+03   -3.41E-03

2.02E-02   1.94E-02   2.31E-02   6.79E-02

n= 43- 63   n= 43- 63

4.76E-04   8.76E+02   8.53E-03   3.26E+02   -7.37E-04

5.20E-03   2.86E-03   6.05E-03   1.53E-02

n= 64- 72   n= 64- 72

1.50E-03   1.88E+03   9.24E-03   5.22E+02   -1.43E-03

3.12E-03   4.63E-03   1.11E-02   2.18E-02

n= 73-106   n= 73-106

1.55E-03   1.60E+03   2.86E-04   2.53E+02   -5.45E-04

8.19E-03   9.46E-03   3.87E-03   4.71E-03
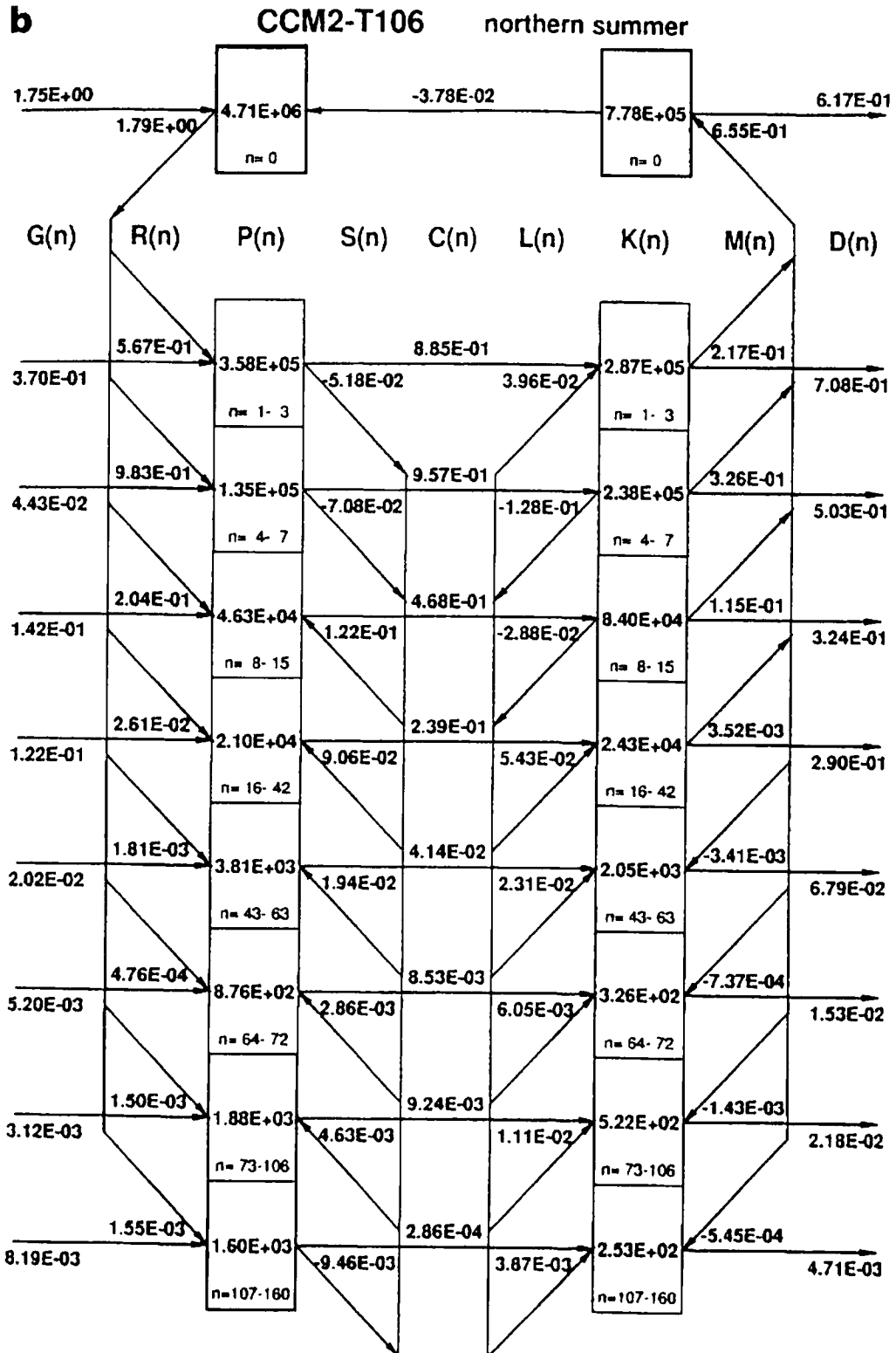
n=107-160   n=107-160

Figure 4.8 *(Continued)*

Another excitation of $K_{(n)}$ is due to the topography as a mechanical forcing in the planetary waves. Accumulated kinetic energy in synoptic and planetary waves is redistributed by the nonlinear wave–wave interactions $L_{(n)}$ to smaller scale motions by means of the downscale energy cascade. A part of the energy cascades upscale to planetary waves as seen for the northern summer. The synoptic and planetary waves accelerate the zonal jet by the barotropic conversion $M_{(n)}$ when the baroclinic waves decay. Hence, the zonal-wave interactions $M_{(n)}$ are from waves to zonal. It is found in this study that the barotropic conversion $M_{(n)}$ is negative for wavenumbers larger than 42. In other words, the short waves beyond the wavenumber 42 are not responsible for the maintenance of the zonal jet. This finding may be important for the model construction, in a sense that T42 is the minimum requirement for the sufficient two-way interactions between eddies and zonal motions. The treatment beyond these wavenumbers may be parameterised by a traditional diffusion process.

4.9   Summary

The objective of the present study is to assess the model's uncertainty associated with the energy transfer in the wavenumber domain. The energy spectrum and energy flows in the wavenumber domain are investigated with high- and low-resolution models over the truncation range of R15, T42, T63 and T106. For validation, we analysed ECMWF global analysis for five years from 1986 to 1990. The effect of the artificial truncation in the wavenumber domain to the energy redistribution of the model atmosphere is discussed in this study.

It is emphasised that the energy spectrum and energy flows, as for both direction and amount, in the CCM2-R15 simulation is much different from those in the higher resolution models. Evidently, it is difficult to employ the R15 model for the studies of climate forecasting. According to the result from T106 simulation, the wave–wave interactions of kinetic energy show an important downscale energy transfer from synoptic scales (wavenumbers 4–15) to short waves. The magnitude of the energy flux in the wavenumber domain toward the short waves are of the order of 0.1 W m^{-2} at the wavenumber 15. This energy transfer is forced as zero in R15 since the energy redistribution by the wave–wave interaction must be accomplished within the resolvable spectral range. Probably, the missing 0.1 W m^{-2} of downscale energy flux in R15 is parameterized by an unrealistically increased diffusion process in order just to draw the necessary amount of energy.

In conjunction with the climate prediction by means of a LAM nested within the GCM such as R15, we can raise a warning of a missing two-way interaction under the LAM-GCM. Suppose we attempt to save the computer resources of T106 climate prediction with a substitution of a nesting of LAM-GCM. Here, the GCM is R15 and the LAM has a resolution comparable to T106. The question is can we obtain a similar climate prediction by these two approaches: one is by T106 (expensive) and the other by LAM-GCM (cheap)? We are almost sure that the answer is no. The important finding in this study is that about 0.1 W m^{-2} of energy transfer has resulted from the complicated two-way interaction of the large- and small-scale motions at the wavenumber 15 in the case of the T106 simulation. This amount

of interaction between the large- and small-scale motions is missing in LAM-R15, and the missing interactions are treated by a prescribed form of a simple diffusion process in R15. The missing energy flux of 0.1 W m^{-2} gives a measure of a residence time of 100 days by which the whole eddy kinetic energy can be replaced. Processing this amount of uncertainty within R15, can we expect a similar climate prediction of the decade ahead as in T106 using the cheap LAM-GCM? It seems that the climate prediction by LAM-R15 may allow a comparable regional resolution as in T106, but is at most a prediction by R15. What we observe with the combination of R15 and LAM is simply the prediction by R15 interpreted with the resolution of the LAM, which should be fundamentally different from the prediction by T106. The utility of the LAM-GCM depends on the application of this nesting approach. When the nesting approach is used for a short-term weather prediction, the method should work perfectly as seen in daily operational forecasting. Even for a climate study, the method of nesting will be a valuable one when it is used for a process study, for example, sea-ice dynamics and feedback process study by Lynch et al. (1995). Here, the LAM is used to help to understand the reaction of the meso-scale phenomena in the Arctic, such as arctic surface, sea-ice, lead and polynia, against a forcing by large-scale motions. The regional climate prediction, however, depends on an equilibrium of the complicated two-way interaction between the large and small. Therefore, the application to a regional climate prediction needs a further scientific basis.

The improvements from R15 to T42 resolution models are significant. The characteristics of the T63 model are similar to those in the T106 simulation. The zonal-wave and wave–wave interactions of kinetic and available potential energies in the T106 simulation, however, tend to transfer more energies into higher wavenumbers than those in the T63 atmosphere. The T42 simulation indicates a notable defect in reproducing the double-jet structure in SH winter. This discrepancy has resulted from the erroneous zonal-wave interactions of kinetic energy, $M_{(n)}$. The T106 simulation also has some defects. For example, the generation of eddy kinetic energy simulated with the T106 model is obviously different from those of the observed. In general, the T63 simulation is comparable to the T106 atmosphere, and in practice, T42 may be sufficient. It is found in this study of the high-resolution model analysis that the barotropic conversion $M_{(n)}$ is negative for wavenumbers larger than 42. In other words, the short waves beyond the wavenumber 42 are not responsible for the maintenance of the zonal jet. This finding may be important for the model construction, in a sense that T42 is the minimum requirement for the sufficient two-way interactions between eddies and zonal motions. The treatment beyond these wavenumbers may be parameterized by a traditional diffusion process.

Acknowledgments

References

Giorgi, F. and Mearns, L.O. (1991) Approaches to the simulation of regional climate change: A review. *Review of Geophysics*, **29**, 191–216.

Hack, J.J., Boville, B.A., Briegleb, B.P., Kiehl, J.T., Rasch, P.J. and Williamson, D.L. (1993) Description of the NCAR community climate model (CCM2). Technical Report NCAR/TN-328+STR, NCAR.

Hasegawa, A. (1995) Comparative energetics of the climate models with high and low resolutions. *Masters Thesis*, Graduate Program in Geoscience, University of Tsukuba.

Kida, H., Koide, T. , Sasaki, H. and Chiba, M. (1991) A new approach for coupling a limited area model to a GCM for regional climate simulations. *Journal of the Meteorological Society of Japan*, **69**, 723–728.

Kung, E.C. and Tanaka, H.L. (1983) Energetics analysis of the global circulation during the special observation period of FGGE. *Journal of Atmospheric Science*, **40**, 2575–2592.

Kung, E.C. and Tanaka, H.L. (1984) Spectral characteristics and meridional variations of energy transformations during the first and second special observation periods of FGGE. *Journal of Atmospheric Science*, **41**, 1836–1849.

Kung, E.C. (1988) Spectral energetics of the general circulation and time spectra of transient waves during the FGGE year. *Journal of Climate*, **1**, 5–19.

Lynch, A.H., Chapman, W.L., Walsh, J.E. and Weller, G. (1995) Development of a regional climate model of the western Arctic. *Journal of Climate*, **8**, 1555–1570.

Lorenz, E.N. (1955) Available potential energy and the maintenance of the general circulation. *Tellus*, **7**, 157–167.

Matsuno, T. (1980) Lagrangian motion of air parcels in the stratosphere in the presence of planetary waves. *Pure Application in Geophysics*, **118**, 189–216.

Ogasawara, N. (1995) Comparative study of the spectral energetics of the general circulation with JMA, NMC and ECMWF global analyses. *Graduate Thesis*, University of Tsukuba.

Oort, A.H. (1964) On estimates of the atmospheric energy cycle. *Monthly Weather Review*, **92**, 483–493.

Saltzman, B. (1957) Equations governing the energetics of the large scales of atmospheric turbulence in the domain of wavenumber. *Journal of Meteorology*, **14**, 513–523.

Saltzman, B. (1970) Large-scale atmospheric energetics in the wavenumber domain. *Review in Geophysical Space Physics*, **8**, 289–302.

Tanaka, H.L. and Kimura, K. (1996) Normal mode energetics analysis and the intercomparison for the recent ECMWF, NMC and JMA global analyses. *J. Meteor. Soc. Japan*, **74**, 525–538.

Williamson, G.S. (1993) CCM2 datasets and circulation statistics. Technical Report NCAR/TN-391+STR, NCAR.